Journal of
Materials Chemistry A

This article can be cited before page numbers have been issued, to do this please use: Y. Zeng, C. Liu, L. Wang, S. Zhang, Y. Ding, Y. Xu, Y. Liu and S. Luo, *J. Mater. Chem. A*, 2016, DOI: 10.1039/C6TA07397B.

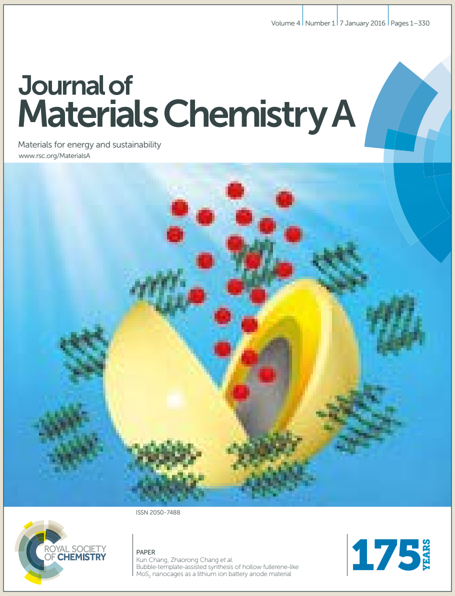

View Article Online
DOI: 10.1039/C6TA07397B

Journal Name

ARTICLE

Three-dimensional graphitic carbon nitride belt network for enhanced visible light photocatalytic hydrogen evolution

Received 00th January 20xx,
Accepted 00th January 20xx

DOI: 10.1039/x0xx00000x

www.rsc.org/

Yunxiong Zeng[a], Chengbin Liu[a,]*, Longlu Wang[a], Shuqu Zhang[a], Yangbin Ding[a], Yuzi Xu[a], Yutang Liu[b], Shenglian Luo[a,]*

Three-dimensional (3D) network-like graphitic carbon nitride nanobelt (g-C_3N_4 NB) was facilely achieved by hydrothermal treatment of bulk g-C_3N_4 in a medium strong oxalic acid solution (1M, pH 0.89). The conduction (CB) and valence band (VB) level position was upraised from -0.90, +1.86 eV for bulk g-C_3N_4 to -0.92, +1.92 eV respectively for g-C_3N_4 NB networks with enhanced redox ability. With optimized Pt loading of 3%, g-C_3N_4 NB networks showed an excellent visible-light photocatalytic H_2 production activity (1360 $\mu mol\cdot g^{-1}\cdot h^{-1}$), which was 10.9 times higher than that of optimized 2% Pt@bulk g-C_3N_4 (124.7 $\mu mol\cdot g^{-1}\cdot h^{-1}$) with triethanolamine as a sacrificial agent. Furthermore, Pt@g-C_3N_4 NB exhibited a considerable rate of H_2 evolution of 33.3 $\mu mol\cdot g^{-1}\cdot h^{-1}$, much higher than 1.79 $\mu mol\cdot g^{-1}\cdot h^{-1}$ for Pt@bulk g-C_3N_4 in distilled water without any sacrificial agents, revealing a great potential of photocatalytic overall water splitting. This outstanding performance not only originated from unique 3D nanostructure and prolonged electron lifetime, but also electronic structure modulation and improved redox capacities of CB and VB. The pH effect of hydrothermal conditions on g-C_3N_4 molecular structure, chemical elelment, optical properties and catalytic performance was expounded. This study demonstrates a facile and environment-friendly strategy to design highly efficient g-C_3N_4 catalysts for potential applications in solar energy photocatalytic water splitting.

Introduction

Increasing enormous fossil energy consumption has driven human to seek highly efficient catalysts with the purpose of converting sustainable solar energy into renewable, green and carbon-free hydrogen fuel via hydrogen evolution reaction (HER) from photocatalytic water splitting.[1,2] In the multitudinous semiconductor catalysts, g-C_3N_4 as a fascinating metal-free visible-light responsive photocatalyst has aroused extensive concern owing to its unique features including abundance, cheapness, nontoxicity, stability and chemical tenability.[3,4] However, the pristine g-C_3N_4 prepared by thermal condensation of nitrogen-rich organic precursors still suffers from unsatisfactory photocatalytic efficiency due to its bulky structure, poor light absorbance, rapid recombination of charge carriers and inadequate catalytic sites.[5,6] In this regard, numerous modification approaches have been proposed to promote its catalytic performance including electronic structure modulation,[7,8] crystal-structure engineering,[9] nano-structure design[10-12] and heterostruction construction.[13,14]

Nanostructure strategy is considered as one of facile, diverse, flexible and efficient approaches to obtain g-C_3N_4 photocatalyst with morphological features, unique electronic structures, strong optical response and functional surface properties.[12,15] The photocatalytic HER at catalyst/water interface highly depend on the size, morphology, and surface property of catalysts.[16,17] As we all know, one-dimension (1D) material has unique advantages in electron transfer along prescribed direction and far away from agglomeration compared with 2D sheets.[18,19] 3D structure from assembly of 1D units possesses the biggest light capacity, largest surface area, maximum exposure of active sites, and least mass transportation resistance.[20,21] In the nanostructure engineering strategy family, template-assistance approach, top-down strategy and solvothermal technology have been perceived as representative and effective means to prepare multidimensional g-C_3N_4 nanostructures.[22,23] However, the use of hazardous fluoride-contained reagents, shortage of template species and side effect of carbon residues limit template approach application.[24,25] In comparison, soft solution-processing approach allows for the bottom-up design of g-C_3N_4 structure in a one-pot manner by solution assembly, crystallization, and covalent cross-linking chemistry.[23,26] Only relying on structure-controlled technique is insufficient and the modulation of energy-band configuration of g-C_3N_4 is needed to strengthen light absorption and redox potentials.[27] The control of morphology and modulation of energy band position in one step process has been rarely studied up to now.

---

[a] State Key Laboratory of Chemo/Biosensing and Chemometrics, Hunan University, Changsha 410082, P. R. China. *E-mail: chem_cbliu@hnu.edu.cn (C. Liu); sllou@hnu.edu.cn (S. Luo)
[b] College of Environmental Science and Engineering, Hunan University, Changsha 410082, P. R. China.

View Article Online
DOI: 10.1039/C6TA07397B

In this study, the 3D network-like morphology of g-C_3N_4 NB could be facilely obtained in hydrothermal treatment of bulk g-C_3N_4 in a medium strong oxalic acid solution (1mol/L, pH 0.89). At first, g-C_3N_4 molecules were tailored by proton in the -N(C)$_3$ bond position, then small molecular weight g-C_3N_4 were spontaneously self-assembly into 3D network-like nanobelt structure (Scheme 1). Furthermore, the modulation of energy-band position was synchronously achieved by introducing oxygen-contained functional groups to g-C_3N_4 and quantum confinement effect. Meanwhile, insightfully understanding nanoarchitectural g-C_3N_4 formation mechanism, optical properties and effect of various oxidized state on catalytic performance was expounded systematically in N_2H_4 (pH 13.72, 80 vol%), $NH_3 \cdot H_2O$ (pH 11.35, 20 wt%) and distilled water (pH 6.86) experiments, respectively. In particular, 3D network-like g-C_3N_4 NB exhibited preeminent visible-light photocatalytic HER, as well as powerful redox capacity, both in triethanolamine (TEOA) solution and pure water overall splitting. This study demonstrates a facile and environment-friendly strategy to design to develop highly-efficient g-C_3N_4.

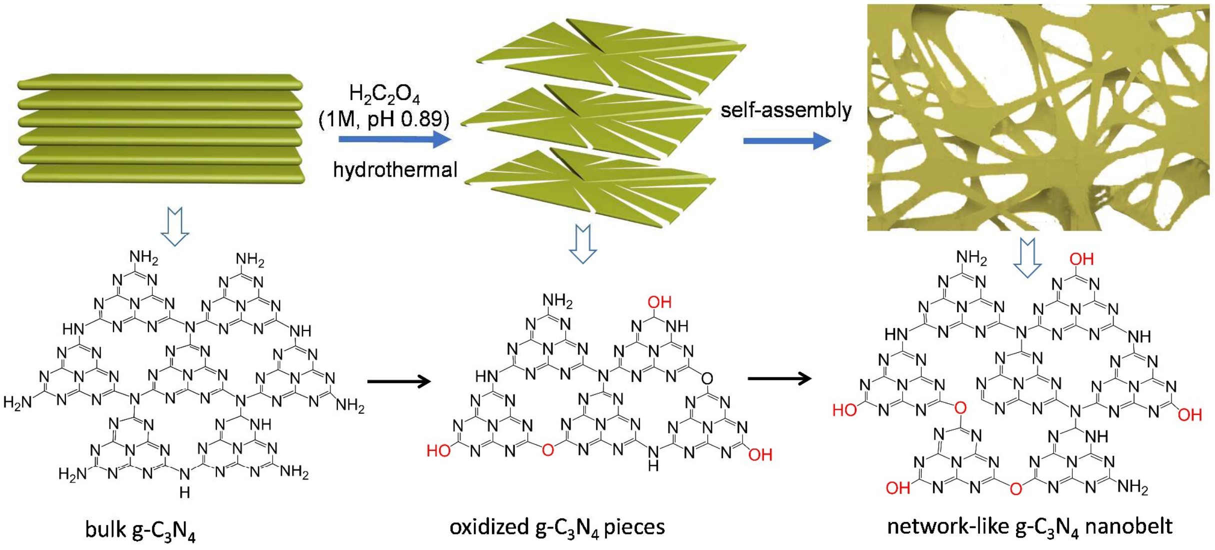

Scheme 1. Illustration for the formation mechanism of g-C_3N_4 nanobelt network.

Experimental

Chemicals

Melamine ($C_3H_6N_6$) was purchased from Tianjin Damao Chemical Reagent. Oxalic acid ($H_2C_2O_4$) was bought from Tianjin Gaungfu Chemical Reagent. Chloroplatinic acid ($H_2PtCl_6 \cdot H_2O$), standard $KMnO_4$ solution (0.02M), potassium biphthalate ($C_8H_5KO_4$) were purchased from Sinopharm Chemical Reagent. Tri-ethylamine (TEOA, $(C_2H_5)_3N$), H_2O_2 (ca. 30 wt%) solution, potassium iodide (KI, 0.4M) hydrazine hydrate (N_2H_4, 80 vol%) solution and concentrated ammonia solution ($NH_3 \cdot H_2O$, 20 wt%) were all purchased from Sinopharm Chemical Reagent Co. Ltd. All the reagents analysis graded and without purification. Distilled water was used in the whole experiment process.

bulk parent g-C_3N_4 preparation

Five grams of melamine powder in an alumina crucible were heated to 550°C from room temperature in a tube furnace at a heating rate of 2.5°C/min under ambient pressure in air, and kept for 4 h at 550°C. The light yellow g-C_3N_4 sample was obtained after natural cooling and then ground into powder g-C_3N_4.

Preparation of g-C_3N_4 nanobelt network.

Firstly, a suspension of bulk g-C_3N_4 (0.46 g) in 50 mL of saturated $H_2C_2O_4$ solution (pH=0.89, 1.0M) was stirred for 12 hours at room temperature following vigorous sonication for 4 hours. Then, the suspension above after removal of solid at the bottom was subjected to hydrothermal treatment in an oven at 160°C for 24 h. The solid in the suspension was separated by centrifugation, then washed with distilled water, ethanol absolute and acetone for three times, and finally dried at 80°C for 24 h. The obtained g-C_3N_4 nanobelts were abbreviated as g-C_3N_4 NB (51% in yield). Additionally, highly oxidized carbon nitride nanofibers (OCN NF, 7.2% in yield), highly oxidized carbon nitride nanocluster (OCN NC, 9.3% in yield) and g-C_3N_4 nanoneedles (g-C_3N_4 NN, 65% in yield) were prepared under the same conditions as in g-C_3N_4 NB preparation only using N_2H_4 (pH=13.72, 80 vol%), concentrated $NH_3 \cdot H_2O$ (pH=11.35, 20 wt%) and distilled water (pH=6.86) to replace $H_2C_2O_4$, respectively.

Pt@g-C_3N_4 preparation

View Article Online
DOI: 10.1039/C6TA07397B

Pt was in situ photodeposited on the g-C_3N_4 samples in 10 vol% triethanolamine and H_2PtCl_6 solution using a full arc light (λ> 300 nm) for 2 h. Before irradiation, the system was bubbled with nitrogen for 30 min to remove the air ensuring the reaction system in an inertial condition. The Pt content was adjusted with H_2PtCl_6 concentration and reaction time and determined by inductively coupled plasma (ICP, PE5300DV).

Characterization

The morphologies and chemical composition characterization of the g-C_3N_4 samples were performed using powder X-ray diffraction (XRD) with Cu-Kα radiation (Rigaku, Smartlab), Fourier transform infrared (FTIR) spectra on a Nicolet 380 (Thermo Fisher Scientific), Transmission electron microscopy (TEM) (JEOL, JEM-2100F), field emission scanning electron microscopy (FE-SEM) (Hitachi, S-4800), and X-ray photoelectron spectroscopy (XPS) with Al-Kα radiation (Thermo Fisher Scientific, England). The specific surface areas were determined by Brunauer-Emmett-Teller (BET) method with N_2 adsorption at 77 K (BELSORP-mini II). The UV–vis diffuse-reflectance spectra (DRS) were performed on a UV–vis spectrophotometer (Cary 300, Varian) with an integrating sphere. The photoluminescence (PL) spectra at zero bias potential were recorded with Hitachi F-7000 fluorescence spectrophotometer. The time-resolved transient photoluminescence (TRPL) spectrum was performed using Hamamatsu universal streak camera C10910. The chemical element compositions were analyzed by energy dispersive spectrometer (EDS) mapping on a Tecnai G2 F20 S-TWIN atomic resolution analytical microscope. The photocurrents of the samples were carried out on a CHI 660C electrochemical analyzer (CHI Inc., USA) in 0.5 M Na_2SO_4 aqueous solution using a three-electrode configuration with a sample-deposited fluorine-doped tin oxide (FTO) electrode as the photoanode, a platinum wire as the counter electrode, and a saturated calomel electrode (SCE) as the reference electrode. All the samples were analyzed under room temperature without bias potential. A 300 W xenon arc lamp with lighting wavelength range of 320−780 nm (Perfectlight, PLS-SXE 300C, China) was used as light source.

Photocatalytic hydrogen production tests

The photocatalytic hydrogen evolution experiments were performed in an 80 mL sealed quartz flask at 5℃ temperature. A 300 W xenon arc lamp with a 420 nm wavelength cutoff filter (Perfect light, PLS-SXE 300C, China) was used as a visible light source to trigger the photocatalytic reaction. The Xe lamp was positioned 20 cm away from reactor with focused intensity of 160 mW·cm^{-2}. In a typical photocatalytic experiment, 20 mg of photocatalysts were dispersed in an 80 mL aqueous solution containing 10 vol% triethanolamine (TEOA) or in distilled water without any sacrificial agents. Before irradiation, the system was bubbled with nitrogen for 30 min to remove the air ensuring the reaction system in an inertial condition. The hydrogen was analyzed by gas chromatography (Shimazu GC2010) equipped with a thermal conductive detector (TCD) and a 5 A molecular sieve column, using nitrogen as the carrier gas.

Results and discussion

The SEM images of g-C_3N_4 samples are shown in Fig. 1. The bulk parent g-C_3N_4 seriously agglomerated together (Fig. 1a). Obviously, the bulky structure was against light absorption, charge transport and mass transportation. [14,15] When hydrothermal treatment in N_2H_4 solution (pH=13.72), $NH_3·H_2O$ solution (pH=11.35), distilled water (pH=6.86) and saturated $H_2C_2O_4$ solution (pH=0.89), OCN NF (Fig. 1b), OCN NC (Fig. 1c), g-C_3N_4 NN (Fig. 1d) as well as g-C_3N_4 NB network (Fig. 1e and f) were obtained, respectively. It is noted that 3-D g-C_3N_4 belt network nanostructure was for the first time fabricated without template assiatance. The unique 3-D network-like nanostructure is in favour of harvesting light, possessing large surface and decreasing mass transfer resistance.

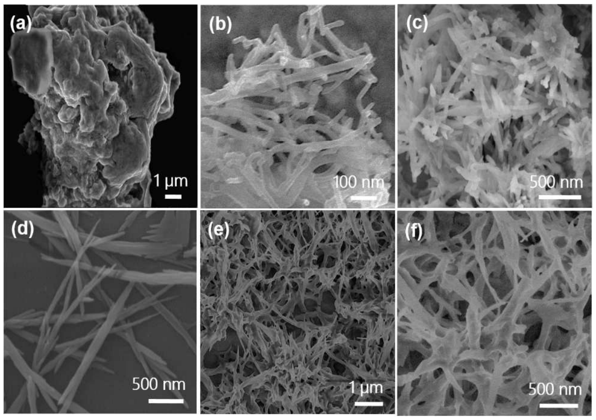

Fig. 1 SEM images of (a) bulk g-C_3N_4, (b) OC_3N_4 NF, (c) OCN NC, (d) g-C_3N_4 NN and (e-f) g-C_3N_4 NB.

The g-C_3N_4 samples were further characterized by FTIR and XRD spectra (Fig. 2). As shown in FTIR spectra (Fig. 2A), all g-C_3N_4 samples displayed typical absorption bands of g-C_3N_4 at 1572 and 1632 cm^{-1} for C=N stretching, at 1253, 1320 and 1425 cm^{-1} for aromatic C-N stretching, and at 810 cm^{-1} for the deformation of tri-s-triazine ring modes. [12,13] Compared with bulk g-C_3N_4, all g-C_3N_4 samples showed stretching vibration of C-O at about 1080 cm^{-1} and broad stretching vibration of hydroxyl (O-H) at 3100-3300 cm^{-1},[26,28] indicative of the introduction of O-contained functional groups. Additionally, both OCN NF and OCN NC exhibited obvious stretching vibration of -NH_2 groups at 3400 cm^{-1} and bimodal coupled vibration of C=O at 1750 cm^{-1} and 1786 cm^{-1}. [27,29]

In the XRD patterns (Fig. 2B), compared with other g-C_3N_4 samples, g-C_3N_4 NB showed much lower diffraction peak intensity at 27.5° (002) assigned to interlayer stacking of g-C_3N_4 sheets,[30,31] implying few layer structure (also confirmed by the TEM result in Fig. 3b). The 13.1° (100) peak was typical inter-planar distance between nitride pores in g-C_3N_4,[32,33] while the peak in g-C_3N_4 NB and g-C_3N_4 NN moved to lower diffraction angle with larger in-plane distance. However, more additional impure peaks appeared in OCN NC, especially in OCN NF, declaring other carbon nitride oxidation mixture existence in addition to bulk pristine g-C_3N_4.[27,29,34] The possible oxidation mechanism of g-C_3N_4 in H^+ (I) and OH^- (II) hydrothermal process was proposed in Scheme 2. Under

View Article Online
DOI: 10.1039/C6TA07397B

alkaline condition, OH^- ions attacked the C atoms with low density of electric charge. Resultantly, the bond deformation of C-N occurred and new primary amine or C=O groups formed. Owing to the destruction of trs-s-triazine, there are a series of deeply oxidized carbon nitride mixtures in addition to pristine g-C_3N_4. In acidulous condition, H^+ ions preferred to attack bridging N atoms with rich electrons, and then OH^- from dissociation of water molecules attacked C atoms adjacent to bridging N atoms. Thus, C-N bond and –OH formed with NH_3 release which was suffocating when opening the reactor lid.

According to the photocatalytic activity of these photocatalysts, g-C_3N_4 NB showed the highest photocatalytic hydrogen production. So the structure of g-C_3N_4 NB was further investigated. Fig. 2C-F show the XPS survey results of bulk g-C_3N_4 and g-C_3N_4 NB. High-resolution C1s for g-C_3N_4 NB shows the standard reference carbon (284.53 eV) and the sp^2-bonded C in N=C(-N)$_2$ (288.09 eV) (Fig 2D) which is well consistent with that of bulk g-C_3N_4.[35-36] The deconvolution of the N 1s XPS signals for g-C_3N_4 NB shows three peaks with binding energies of 398.54, 399.66 and 401.00 eV from sp^2-hybridized N in C-N=C groups, tertiary nitrogen N-(C)$_3$ and the N-H bond in g-C_3N_4, respectively (Fig 2E).[37] O 1s signals show a broad peak at about 531.24 eV corresponding to N-C-O (Fig 2F).[38,39] After hydrothermal treatment, O 1s peak intensity proportional to oxygen content distinctly enhanced more than two fold (Table S1), indicating oxygen-containing functional groups existence in g-C_3N_4 NB.[40,41]

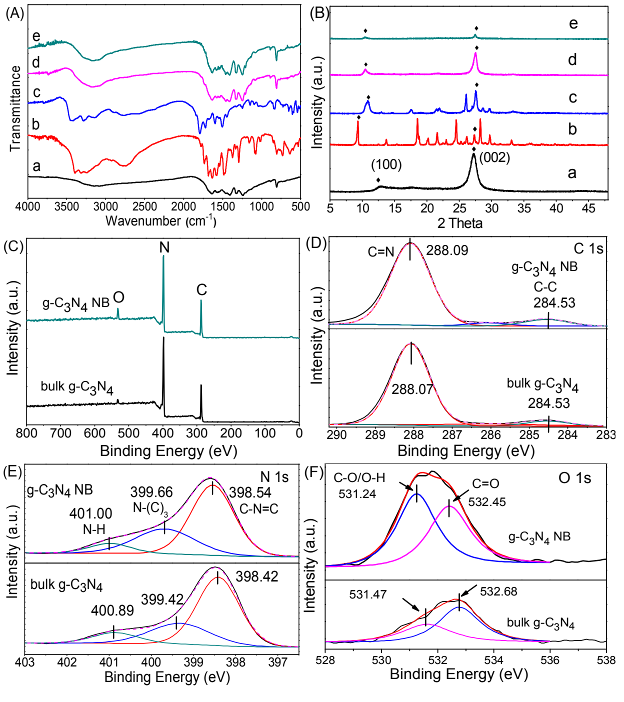

Fig. 2 FTIR spectra (A) and XRD patterns (B) of (a) bulk parent g-C_3N_4, (b) OCN NF, (c) OCN NC, (d) g-C_3N_4 NN, and (e) g-C_3N_4 NB; XPS spectra (C-F) of bulk g-C_3N_4 and g-C_3N_4 NB.

The TEM images show that the g-C_3N_4 nanobelts with a width from 10 to 50 nm and an overlong micron level connected to each other to form a network (Fig. 3a). The HR-TEM image indicated a single or few layer characteristic of nanobelt without edge line gradient (Fig. 3b). Nanobelts were characteristic of overlong, ultrathin and homogeneous shapes with extremely large length to diameter ratio. The distinctive networks composed of 1D ultrathin nanobelts would greatly enhance light harvesting, photo-induced carrier transport and fast mass transfer as well as possess abundant active sites for boosting interface reaction rate.[20,21] The EDX and elemental mapping analysis evidenced the existence of C, N and O elements in g-C_3N_4 NB (Fig. 3d and e).

The photocatalytic HER performance greatly correlated with the specific surface area of catalysts.[42] As shown in Fig. 4 and Table 1, the specific surface areas were 62.7, 42.4, 35.2, 32.5 and 7.0 m^2/g for g-C_3N_4 NB, OCN NF, OCN NC, g-C_3N_4 NN and bulk g-C_3N_4 respectively. The highest specific surface area of g-C_3N_4 NB should result from its unique 3-D network structure composed of ultrathin nanobelts. Clearly, the high specific surface area of g-C_3N_4 NB could offer sufficient reactive sites and accelerate the mass transfer of reactants.

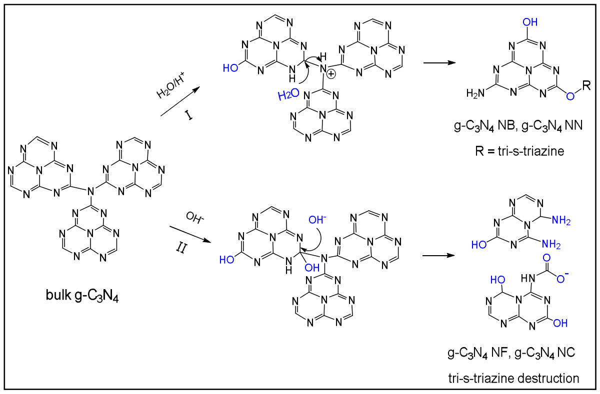

Scheme 2. Proposed oxidation mechanism of g-C_3N_4 in H^+ (I) and OH^- (II) solution.

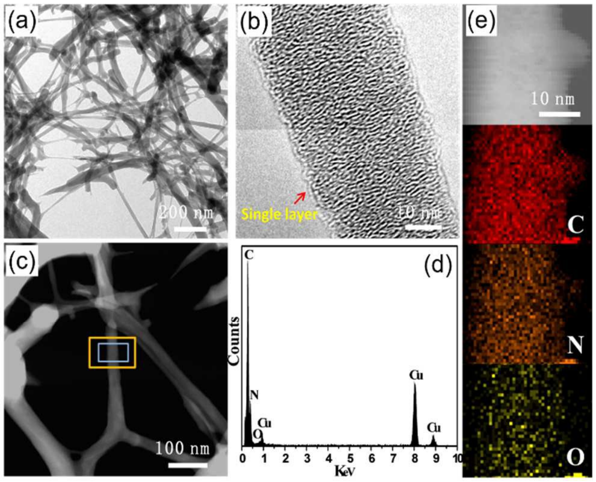

Fig. 3 (a) TEM image of g-C_3N_4 NB, (b) HRTEM image of g-C_3N_4 NB, (c) dark field FESEM-TEM image of g-C_3N_4 NB, (d) EDX spectrum of the indicated area by the yellow box in (c), and (e) elemental mappings of the selected area by blue box in (c).

View Article Online
DOI: 10.1039/C6TA07397B

As shown in DRS spectra (Fig. 5A), compared with bulk g-C_3N_4, all of g-C_3N_4, especially for g-C_3N_4 NB exhibited obvious blue shifts of absorption edges. The blue shift should be attributed to quantum size confinement[43] and the introduction of oxygen-contained groups into g-C_3N_4 which decreased the conjugation length. The band gaps of these g-C_3N_4 materials were calculated using the following formula:

$$\alpha = A(h\nu - Eg)^{n/2}/h\nu$$

where α is the absorption coefficient, A is a constant, h is the Planck's constant, Eg is band energy, ν is the frequency of the incident light, and n is equal to 1 for the direct transition. The calculated bandgap energies were 3.04, 3.02, 2.88, 2.84 and 2.76 eV for OCN NF, OCN NC, g-C_3N_4 NN, g-C_3N_4 NB and bulk g-C_3N_4 (inset in Fig. 5A).

The valence band X-ray photoelectron spectroscopy (VB XPS) was used to further investigate the band gap between g-C_3N_4 NB and bulk g-C_3N_4. Fig. 5B illustrates that the VB of g-C_3N_4 NB positively shifted from +1.86 eV of bulk g-C_3N_4 to +1.92 eV. N2p orbital energy contributes to the main energy of VB for g-C_3N_4, thus, VB up-shifting phenomenon was mainly ascribed to O2p orbital energy higher than that of N2p. According to the band gaps of 2.84 eV for g-C_3N_4 NB and 2.76 eV for bulk g-C_3N_4 calculated from DRS results, the CB level of g-C_3N_4 NB and bulk parent g-C_3N_4 were -0.92 eV and -0.90 eV, respectively. Undoubtedly, more negative CB and positive VB could be endowed more powerful redox ability of g-C_3N_4 NB.

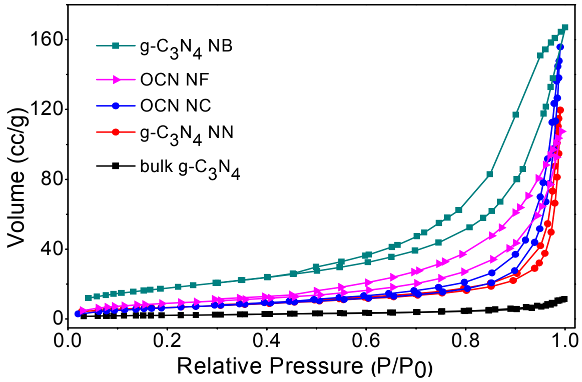

Fig.4 BET N_2 adsorption/desorption isotherms of bulk g-C_3N_4, OCN NF, OCN NC, g-C_3N_4 NN, and g-C_3N_4 NB.

Table 1 Specific surface area of samples.

Samples	bulk g-CN	g-CN NB	g-CN NN	OCN NC	OCN NF
area (m^2/g)	7.0	62.7	32.5	35.2	42.4

Photocurrent is useful for revealing the efficiency of the separation of photoexcited electrons and holes (Fig. 5C). The g-C_3N_4 NB exhibited a photocurrent density of 0.67 μA cm^{-2}, much higher than 0.20 μA cm^{-2} for bulk g-C_3N_4, 0.41 μA cm^{-2} for g-C_3N_4 NN, 0.18 μA cm^{-2} for OCN NC and 0.11 μA cm^{-2} for OCN NF. The low photocurrent intensities of OCN NC and OCN NF implied less excited electrons, possibly resulting from the serious destruction of heptazine ring during hydrothermal process in alkaline solution consistent with FTIR and XRD records. That is to say, by alkaline hydrothermal treatment in concentrated alkaline N_2H_4 or $NH_3 \cdot H_2O$ solution, the pristine C=N covalent bond of g-C_3N_4 was more easily destroyed.

The light-triggered charge separation/recombination rates of the samples were further investigated by photoluminescence (PL) spectra (Fig. 6). Obviously, the change of fluorescence emission wavelength of the samples was consistent with that of absorption wavelength. Both g-C_3N_4 NB and g-C_3N_4 NN exhibited almost equal light absorption capacity to bulk g-C_3N_4 (Fig. 5A), but lower PL intensity than bulk g-C_3N_4 (Fig. 6a), indicative of reduced recombination of photogenerated charge carriers in g-C_3N_4 NB and g-C_3N_4 NN. It is noted that both OCN NF and OCN NC showed lower PL intensity than bulk g-C_3N_4 (Fig. 6a), which could be explained by the fact that less electrons were excited in OCN NF and OCN NC, resulting from low light absorption capacity (Fig. 5A). The fluorescence decay curves exhibited deviation from the third order exponential decay and g-C_3N_4 NB showed slower decay kinetics in contrast to bulk g-C_3N_4, meaning longer lifetime of charge carriers in g-C_3N_4 NB (Fig. 6b).

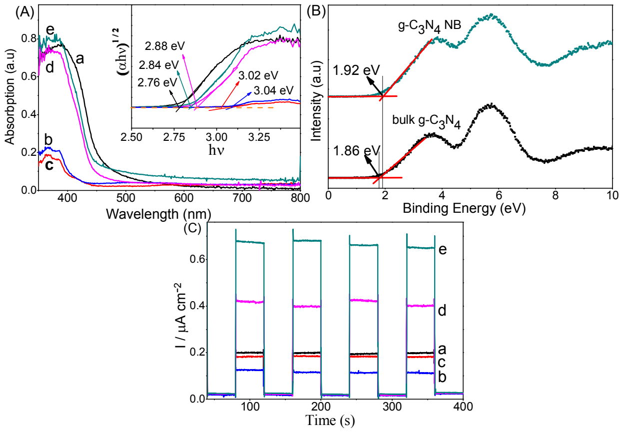

Fig. 5 (A) DRS spectra of the samples, (B) VB XPS spectra of bulk g-C_3N_4 and g-C_3N_4 NB, and (C) photocurrent responses of the samples: (a) bulk g-C_3N_4, (b) OCN NF, (c) OCN NC, (d) g-C_3N_4 NN and (e) g-C_3N_4 NB.

Table 2 summarizes the fluorescence decay changes. The shortest lifetime of 0.78 ns in bulk g-C_3N_4 increased up to 1.17 ns in g-C_3N_4 NB while its percentage of charge carriers decreased from 41.52% to 34.48%. Both the secondary lifetime and percentage of charge carriers augmented from 4.61 ns and 48.16% in bulk g-C_3N_4 to 5.70 ns and 55.58% in g-C_3N_4 NB. What's more, the longest lifetime of 26.14 ns in bulk lengthened to 36.82 ns in g-C_3N_4 NB at a small cost of the shortening percentage only by 0.37%. After multi-exponential fitting, the radiative lifetimes of bulk g-C_3N_4 and g-C_3N_4 NB were 1.43 ns and 2.67 ns, respectively. The time-resolved fluorescence illuminates that the radiative lifetime of charge was distinctly prolonged with the transformation from bulk g-C_3N_4 to g-C_3N_4 NB. The lifetime prolongation of charge carriers acted as an indispensable role in improving photocatalytic reactions before recombination.[44,45] It is believed that the increased lifetime of charge carriers is associated with electron transport improvement and electronic structure change induced by quantum confinement effect or/and electron-drawing effect of oxygen-contained functional groups.

View Article Online
DOI: 10.1039/C6TA07397B

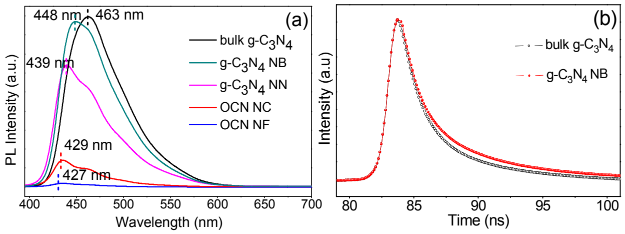

Fig. 6 (a) Fluorescence emission spectra of the samples and (b) time-resolved fluorescence excited by the incident light of 330 nm over bulk g-C_3N_4 and g-C_3N_4 NB.

Table 2 Dynamics analysis of emission decay of bulk g-C_3N_4 and g-C_3N_4 NB.

Samples	A_1[%]	τ_1[ns]	A_2[%]	τ_2[ns]	A_3[%]	τ_3[ns]	τ_A[ns]
bulk g-C_3N_4	41.52	0.78	48.16	4.61	10.32	26.14	1.43
g-C_3N_4 NB	34.48	1.17	55.58	5.70	9.95	36.82	2.67

Fig. 7a presents HER of g-C_3N_4 NB with different Pt loading under visible light irradiation (λ > 420 nm) using TEOA as sacrificial agent. The g-C_3N_4 NB without Pt as cocatalyst showed negligible H_2 production, while the g-C_3N_4 NB catalysts with Pt as cocatalyst exhibited significantly enhanced H_2 generation. With increasing Pt loading from 1 to 3%, the HER rate over Pt@g-C_3N_4 NB obviously increased. When further increasing Pt loading to 4 wt%, the HER rate decreased. The low HER rate over low Pt loading (1 or 2 wt%) should be due to less active sites while HER decrease over higher Pt loading (4 wt%) may be for the fact that excessive cocatalyst blocked photo-excited electrons transfer and reduced active site exposure due to highly overlapping each other.[46,47] For bulk g-C_3N_4, the optimized Pt loading is 2 wt% with an HER production rate of 0.12 mmol·g^{-1}·h^{-1} (Fig. S1). The HER rate over 3 wt% Pt@ g-C_3N_4 NB reached 1.36 mmol·g^{-1}·h^{-1} which is 10.9 times higher than that for 2 wt% Pt@bulk g-C_3N_4.

Fig. 7b shows the photocatalytic HER efficiencies over different photocatalysts with 3wt% Pt. The average H_2 production rate over g-C_3N_4 NB was 1.36 mmol·g^{-1}·h^{-1}, higher than 0.57 mmol g^{-1}·h^{-1} over g-C_3N_4 NN, 0.11 mmol·g^{-1}·h^{-1} over bulk g-C_3N_4, 0.09 mmol·g^{-1}·h^{-1} over OCN NC, and 0.06 mmol·g^{-1}·h^{-1} over OCN NF. Poor catalytic activity of OCN NF and OCN NC inferior to that of bulk g-C_3N_4 indicated active unit tri-s-triazine was deeply destroyed into inactive fragments in hydrothermal alkalic solution, while acid and neutral environment enhanced it activity seen in Scheme 2. The recoverability is also an important consideration for its practical application of one photocatalyst. The photocatalytic activity stability of Pt@g-C_3N_4 NB was evaluated by recycling the photocatalyst towards HER. After five cycles lasting 25 hours, the H_2 production rates remained highly stable under visible light illumination (Fig 7c). The apparent quantum efficiency (AQE) for Pt@ g-C_3N_4 NB reached to 12% at 420 nm (see the calculation in Supplementary Information). The high H_2 production rate and AQE presents one of the best HER performances of g-C_3N_4-based photocatalysts (Table S2). Noteworthily, without using any sacrifice agents, Pt@g-C_3N_4 NB displayed a considerable rate of H_2 production of 33.3 μmol·g^{-1}·h^{-1} under visible light irradiation, 18.6 times higher than 1.79 μmol·g^{-1}·h^{-1} for Pt@bulk g-C_3N_4 (Fig. 7d). Meanwhile, the H_2O_2 production rates are 3.48 μmol·L^{-1}·h^{-1} in the former and 0.29 μmol·L^{-1}·h^{-1} in the latter (Fig. S3), implying the potential of overall water splitting.

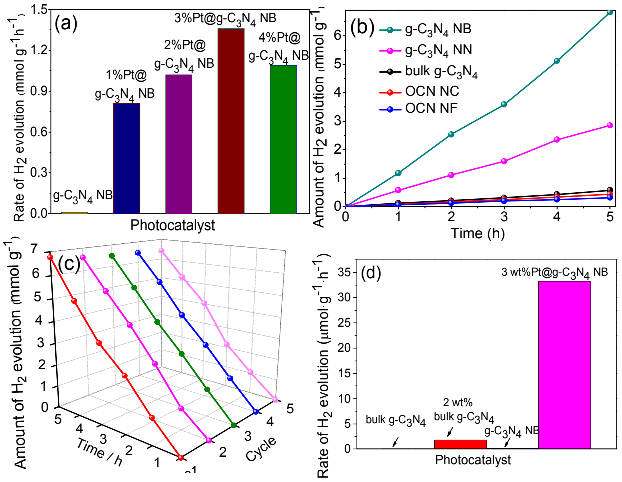

Fig. 7 (a) HER of g-C_3N_4 NB loaded with Pt, (b) 3 wt% Pt@g-C_3N_4 photocatalysts, (c) cycling runs of 3 wt% Pt@g-C_3N_4 NB and (d) HER in distilled water without any sacrificial agents (λ>420 nm). Reaction condition in (a-c): 10 vol% TEOA under visible light irradiation (λ>420 nm).

The photocatalytic HER mechanism over Pt@g-C_3N_4 NB under visible light illumination is proposed as Scheme 3. Under irradiation, the electrons in the valence band (VB) of g-C_3N_4 were excited to its conduction band (CB), and then transfered to Pt for protons reduction. The generated holes in the VB (+1.92 eV) more forcefully oxidized TEOA and H_2O molecule into oxidation products, such as H_2O_2, than that of bulk (+1.86 eV). The more negative CB level of g-C_3N_4 NB (-0.92 eV) than that of bulk parent g-C_3N_4 (-0.90 eV) enhanced the reduction ability of g-C_3N_4 NB. Obviously, the 3D network-like architecture not only maximally boosted light harvesting and offered more active sites but also reduced recombination rate of photo-induced h^+-e^- pairs and acclerated mass transfer at catalytic interface.

View Article Online
DOI: 10.1039/C6TA07397B

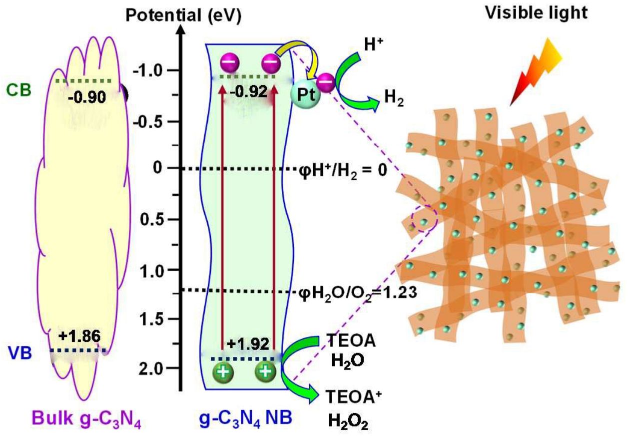

Scheme 3 Illustration of proposed charge transfer in Pt@g-C_3N_4 NB under visible-light irradiation.

Conclusions

In this study, a 3D g-C_3N_4 nanobelt network was facilely achieved by hydrothermal treatment of bulk g-C_3N_4 in saturated $H_2C_2O_4$ solution. Furthermore, the modulation of electronic structure with enhanced redox ability was achieved by introducing oxygen-contained groups to g-C_3N_4 NB. The g-C_3N_4 NB networks showed a high visible-light photocatalytic HER activity and AQE. Notedly, g-C_3N_4 NB networks displayed a considerable rate of H_2 production in water without using sacrifice agent. This study demonstrates a facile and environment-friendly strategy to design highly-efficient g-C_3N_4 catalysts for potential application in solar energy photocatalytic water splitting.

Acknowledgements

This work was supported by Hunan Provincial Natural Science Foundation of China (14JJ1015), the National Natural Science Foundation of China (51572077, 51478171 and 51378187), and Program for Innovation Research Team in University (IRT1238).

Notes and references

1 D. Voiry, J. Yang and M. Chhowalla, *Adv. Mater.,* 2016 DOI: 10.1002 /adma.201505597.
2 X. Zou and Y. Zhang, *Chem. Soc. Rev.,* 2015, **44**, 5148-5180.
3 Q. P. Lu, Y. F. Yu, Q. L. Ma, B. Chen and H. Zhang, *Adv. Mater.,* 2016, **28** 1917-1933.
4 X. Wang, K. Maeda, A. Thomas, K. Takanabe, G. Xin, J. M. Carlsson, K. Domen and M. Antonietti, *Nat. Mater.,* 2009, **8**, 76-80.
5 S. Cao, J. Low, J. Yu and M. Jaroniec, *Adv. Mater.*, 2015, **27**, 2150-2176.
6 T. Xiong, L. Wang, W. Ceng, Y. Zhang and F. Dong, *ACS Catal.,* 2016, **6**, 2462-2472.
7 G. Zhang, M. Zhang, X. Ye, X. Qiu, S. Lin and X. Wang, *Adv. Mater.,* 2014, **26**, 805-809.
8 Z. Lin and X. Wang, *Angew. Chem. Int. Ed.,* 2013*,* **125**, 1779-1782.
9 K. Schwinghammer, M. B. Mesch, V. Duppel, C. Ziegler, J. Senker and B. V. Lotsch, *J. Am. Chem. Soc.,* 2014*,* **136**, 1730-1733.
10 Q. Liang, Z. Li, Z. H. Huang, F. Kang and Q. H. Yang, *Adv. Funct. Mater.,* 2015*,* **25**, 6885-6892.
11 Q. Han, B. Wang, J. Gao and L. Qu, *Angew. Chem. Int. Ed.,* 2016*,* **55**, 1-6.
12 Y. Zheng, L. Lin, X. Ye, F. Guo and X. Wang, *Angew. Chem. Int. Ed.,* **2014**, 53, 11926-11930.
13 J. Tian, L. Zhang, X. Fan, Y. Zhou, M. Wang, R. Cheng, X. Kan, X. Jin, Z. Liu, Y. Gao and J. Shi, *J. Mater. Chem. A,* 2016, DOI: 10.1039/C6TA04297J.
14 T. R. Chetia, M. S. Ansari and M. Qureshi, *J. Mater. Chem. A,* 2016, **4**, 5528-5541.
15 T. Y. Ma, Y. Tang, S. Dai and S. Z. Qiao, *Small,* 2014, **10**, 2382-2389.
16 S. Chen, S. Shen, G. Liu, Y. Qi, F. Zhang and C. Li, *Angew. Chem. Int. Ed.*, 2015, **54**, 3047-3051.
17 J. Yang, D. Wang, H. Han and C. Li, *Acc. Chem. Res.,* 2013, **46**, 1900-1909.
18 C. Liu, L. Wang, Y. Tang, S. Luo, Y. Liu, S. Zhang, Y. Zeng and Y. Xu, *Appl. Catal. B Environ.,* 2015, **164**, 1-9.
19 H. Hou, F. Gao, L. Wang, M. Shang, Z. Yang, J. Zheng and W. Yang, *J. Mater. Chem. A,* 2016,4, 6276-6281.
20 L. Wang, X. Duan, G. Wang, C. Liu, S. Luo and S. Zhang, *Appl. Catal. B Environ.*, 2016,**186**, 88-96.
21 J. Wang, J. Liu, H. Yang, Z. Chen, J. Lin, and Z. X. Shen, *J. Mater. Chem. A*, 2016, ***4***, 7565-7572.
22 Q. Xiang, B. Cheng and J. Yu, *Angew. Chem. Int. Ed.,* 2015, **54**, 11350-11366.
23 Q. Cu, Y. Liao, J. Long, X. Wang and C. Xue, *Appl. Catal. B Environ.,* 2015, **165**, 503-510.
24 J. Zhang, Y. Chen and X. Wang, *Energy. Environ. Sci.,* 2015, **8**, 3092-3108.
25 Y. Zheng, J. Liu, J. Liang, M. Jaroniec and S. Z. Qiao, *Energy. Environ. Sci.*, 2012, **5**, 6717-6731.
26 Q. Gu, Z. Gao and C. Xue, *Small,* 2016, **26**, 3543-3549.
27 L. Ming, H. Yue, L. Xu and F. Chen, *J. Mater. Chem. A,* 2014, **2**, 19145-19149.
28 D.S. Hall, D.J. Lockwood, S. Poirier, C. Bock and B. R. MacDougall, *J. Phys. Chem. A*, 2012, **116**, 6771-6784.
29 K. Zhang, L. Wang, X. Sheng, M. Ma, M. S. Jung and W. Kim, *Adv. Energy Mater.*, 2016, **11**, 1-7.
30 Y. Hou, Z. Wen, S. Cui, X. Feng and J. Chen, *Nano Lett.,* 2016, **16**, 2268-22677.
31 Q. Cui, J. Xu, X. Wang, L. Li, M. Antonietti and M. Shalom, *Angew. Chem. Int. Ed.,* 2016, **55**, 3672-3676.
32 D. H. Wang, J. N. Pan, H. H. Li, J. J. Liu, Y. B. Wang, L. T. Kang and J. N. Yao, *J. Mater. Chem. A,* 2016, **4**, 290–29.
33 X. Bai, C. Sun, S. Wu and Y. Zhu, *J. Mater. Chem. A,* 2015, **3**, 2741–2747.
34 Y. Yuan, L. Zhang, J. Xing, M. I. Utama, X. Lu and K. Du, *Nanoscale,* 2015, **7**, 12343-12350.
35 W. J. Ong, L. L. Tan, S. P. Chai, S. T. Yong and A. R. Mohamed, *Nano Energy,* 2015, **13**, 757-770.
36 Y. Zhou, L. Zhang, W. Huang, Q. Kong, X. Fan and M. Wang, *ACS Appl. Mater. Interfaces,* 2016, **8**, 13879-13889.
37 D. Zheng, X. N. Cao and X. Wang, *Angew. Chem. Int. Ed.,* 2016, **55**, 1–6.
38 X. Chen, Q. Liu, Q. Wu, P. Du, J. Zhu and S. Dai, *Adv. Funct. Mater.,* 2016, **26**, 1719-1728.
39 H. Yu, L. Shang, T. Bian, R. Shi, G.I. Waterhouse and Y. Zhao, *Adv. Mater.,* 2016, DOI: 10.1002/adma.201600398.
40 Y. Jiang, X. Li, T. Wang and C. Wang, *Nanoscale,* 2016, **8**, 9667-9675.
41 C. Xu, Q. Han, Y. Zhao, L. Wang, Y. Li and L. Qu, *J. Mater. Chem. A,* 2015, **3**, 1841-1846.

View Article Online
DOI: 10.1039/C6TA07397B

42 J. Zhang, M. Zhang, C. Yang and X. Wang, *Adv. Mater*., 2014, **26**, 4121-4126.
43 S. Chu, Y. Wang, Y. Guo, J. Feng, C. Wang and W. Luo, *ACS Catal*., **2013**, 3, 912-912.
44 X. She, L. Liu, H. Ji, Z. Mo, Y. Li and L. Huang, *Appl. Catal. B Environ.,* 2016, **187**, 144-53.
45 L. Ma, H. Fan, J. Wang, Y. Zhao, H. Tian and G. Dong, *Appl. Catal. B Environ.,* 2016, 190, **93**-102.
46 D.J. Martin, K. Qiu, S.A. Shevlin, A. D. Handoko, X. Chen and Z. Guo, *Angew. Chem. Int. Ed.,* 2014, **53**, 9240-9245.
47 G. Zhang, C. Huang and X. Wang, *Small,* 2015, **11**, 1215-1221.

View Article Online
DOI: 10.1039/C6TA07397B

Graphical abstract